Design and Analysis of Functionally Graded Materials for Enhanced Thermal Dissipation in EV Battery Packs

Fizza Hasan[1], Hamda Arshad[2], Ghazi Jamal Khan[3], Mohd Umar[4], Sabah Khan[5]
[1,2,3,4,5]*Department of Mechanical Engineering, Faculty of Engineering and Technology, Jamia Millia Islamia, New Delhi 110025, India*

***Abstract*—Electric vehicle (EV) battery packs generate significant heat during charge–discharge cycles, and excessive temperature rise leads to reduced efficiency, accelerated cell aging, and the risk of thermal runaway. This paper presents the design and finite-element analysis of an aluminum–alumina Functionally Graded Material (FGM) intended for use as a thermal-interface and casing element in EV battery packs. A three-dimensional CAD model of a prismatic battery-pack enclosure was developed in SolidWorks, with the FGM stack idealised as five concentric layers of progressively varying composition between pure aluminum and pure alumina. Steady-state thermal and coupled thermo-mechanical analyses were carried out in ANSYS Workbench 2023 R1 across five geometric configurations in which total stack thickness (2.5–7 mm), individual layer thicknesses, and the type of boundary condition (direct temperature versus convection) were systematically varied. The thermal simulations show a strongly non-linear through-thickness gradient with the temperature drop concentrated in the alumina-rich layers; the structural simulations show that peak von-Mises stress (94.1–111.1 MPa) consistently occurs on the aluminum hot face and that an architecture with a thicker alumina bottom layer minimises this peak while keeping all stresses well within the elastic regime of both constituents. The proposed FGM design therefore offers a passive, lightweight, and reliable alternative to active cooling for next-generation EV battery thermal management. Future work will extend the analysis to transient drive-cycle loading, vibration response, and experimental validation of an additively manufactured prototype.**

***Index Terms*— Functionally Graded Materials; EV battery pack; thermal management; ANSYS; SolidWorks; aluminum–alumina; finite element analysis; thermal stress.**

I. INTRODUCTION

The accelerating transition to electric vehicles (EVs) has placed lithium-ion battery packs at the core of automotive engineering. Their performance, longevity, and safety are directly governed by the thermal environment in which they operate. During fast charging and high-rate discharge, individual cells dissipate substantial Joule heat that, if not removed efficiently, drives the pack temperature beyond safe operating limits. Sustained operation above approximately 60 °C is known to accelerate side reactions within the cell, degrade electrolyte stability, and promote uneven aging across cells in the same pack; in extreme cases, it can trigger thermal runaway and the propagating fires that have shaped public perception of EV safety. Conventional thermal-management systems address this challenge through active cooling air, liquid, or refrigerant loops but these systems impose a continuous parasitic load on the vehicle, occupy valuable pack volume, and add weight and mechanical complexity. There is therefore a clear need for passive, integrated thermal-management strategies that dissipate heat without consuming energy and without compromising the structural integrity of the pack.

Functionally Graded Materials (FGMs) are advanced engineered composites in which composition or microstructure varies continuously along a chosen direction, producing a corresponding spatial variation in mechanical, thermal, or chemical properties. By tailoring this variation, an FGM can combine the desirable attributes of two otherwise incompatible materials for example, the high thermal conductivity and ductility of a metal at one face and the heat resistance, stiffness, and electrical insulation of a ceramic at the other. Originally developed in the 1980s

for thermal-protection systems on space vehicles, FGMs have since been investigated for cutting tools, biomedical implants, turbine components, nuclear-reactor parts, and most recently for energy-storage applications, where their ability to manage steep thermal gradients without delamination is particularly valuable.

The present work investigates an aluminum–alumina (Al–Al_2O_3) FGM as a thermal-interface plate within an EV battery pack. Aluminum, with thermal conductivity k = 237 W/m·K, provides rapid heat extraction from the cell surface, while alumina, with k = 30 W/m·K, simultaneously acts as a thermal barrier, an electrical insulator, and a structural skin. By gradually varying the volume fraction of these two phases through the thickness of the plate, the abrupt mismatch in thermal and mechanical properties at a conventional metal–ceramic bi-material interface is replaced by a smoother gradient that reduces both stress concentrations and interfacial heat-flux discontinuities.

1.1 Problem Statement and Objectives

The problem addressed in this paper is to optimize the spatial distribution of thermal conductivity through the wall of an EV battery-pack enclosure such that maximum heat is dissipated from the cell surface while minimizing the thermal stress arising from CTE mismatch and maintaining temperature uniformity, electrical insulation, and structural integrity. The specific objectives are:

- To design a three-dimensional CAD model of a prismatic EV battery-pack enclosure that embeds an FGM thermal-interface stack between the cells and the outer casing.
- To evaluate, through finite-element steady-state thermal analysis, the temperature field developed in candidate FGM layer architectures under representative EV battery operating conditions.
- To evaluate, through coupled thermo-mechanical analysis, the von-Mises stress distribution arising from the thermal-expansion mismatch between layers and any superimposed mechanical clamping load.
- To identify, by comparison across five geometric configurations, the layer architecture that provides the most favourable trade-off between heat dissipation, peak stress, and mechanical compliance.

II. METHODOLOGY

The methodology adopted in this study is summarised in three sequential stages. First, a three-dimensional CAD model of the battery-pack enclosure with an embedded FGM stack was developed in SolidWorks. Second, the geometry was imported into ANSYS Workbench 2023 R1 (Student version) for steady-state thermal finite-element analysis across five layer-architecture cases. Third, the converged temperature field from each thermal case was passed to a coupled Static Structural analysis to evaluate the resulting thermo-mechanical stress field. Each stage is described in detail below.

2.1 CAD Model of the Battery-Pack Enclosure

2.1.1 Cell Selection and Pack Configuration

The external dimensions of the enclosure were derived from a cell-packing study based on the standard 18650 cylindrical lithium-ion format. The 18650 cells, named for its 18 mm diameter and 65 mm height, is the most widely deployed cylindrical Li-ion format in entry-level EVs, electric two-wheelers, and the e-rickshaw segment. Each 18650 cell is assumed to have a nominal voltage of 3.7 V and a nominal capacity of 2.5 Ah, consistent with the values published by leading cell manufacturers.

Taking the enclosure inner-volume dimensions as the constraint, a packing study was carried out to determine how many 18650 cells fit in a rectangular close-packed arrangement. Along the 150 mm width, 150 / 18 ≈ 8 cells fit side-by-side; along the 159 mm length, 159 / 18 ≈ 8 cells fit; and along the 338 mm height, 338 / 65 ≈ 5 cells stack vertically. This yields a maximum capacity of 8 × 8 × 5 = 320 cells, with sufficient remaining clearance for inter-cell insulating spacers, bus-bar routing, and the FGM thermal-interface layer.

The 320 cells are wired in a 16S20P configuration 16 cells connected in series within each parallel group, and 20 such groups connected in parallel which is the standard low-voltage configuration.

The resulting pack-level electrical specifications are obtained directly from the cell-level values: a nominal pack voltage of 16 × 3.7 = 59.2 V, a pack capacity of 20 × 2.5 = 50 Ah, and a total stored energy of approximately 59.2 × 50 ≈ 2960 Wh, i.e. about 3 kWh. This places the design firmly within the 60 V class of e-rickshaw and electric-two-wheeler battery packs that are widely deployed in commercial service, providing

a practical and realistic target geometry for the thermo-mechanical analysis that follows. The external dimensions were specified with general tolerances of ±0.5 mm per DIN ISO 2768-mk (medium class for linear dimensions in the 120–400 mm range), which is conventional for sheet-metal and additively-manufactured enclosure parts. The pack specifications are summarised in Table 1.

Parameter	Value
Cell type	18650 cylindrical Li-ion
Cell dimensions	18 mm diameter × 65 mm height
Nominal cell voltage	3.7 V
Nominal cell capacity	2.5 Ah
Physical arrangement	8 × 8 × 5 (Width × Length × Height)
Total cells	320
Electrical configuration	16S20P (16 series × 20 parallel)
Pack nominal voltage	59.2 V
Pack nominal capacity	50 Ah
Pack stored energy	≈ 2960 Wh (≈ 3 kWh)
External enclosure dimensions	150 × 159 × 338 mm
Dimensional tolerance	±0.5 mm (DIN ISO 2768-mk)

Table 1 Battery pack configuration and electrical specifications used to size the enclosure.

2.1.2 Enclosure Geometry and FGM Layered Construction

Given the pack configuration above, a three-dimensional solid model of the FGM-based battery pack enclosure was developed in SolidWorks 2024 to establish the physical geometry, layer architecture, and spatial arrangement of the FGM stack. The base housing was created by extruding a closed rectangular profile with rounded corner fillets to reduce stress concentrations at the edges, and vertical ribs were added along all four side walls to increase the out-of-plane bending stiffness of the panels without a proportional increase in mass. A separate top cover plate incorporating a connector recess, mounting lugs, and a venting aperture was modelled as an interlocking body to enable removal for cell servicing.

Since SolidWorks does not natively support spatially varying material properties, the continuously graded composition of the enclosure wall was approximated by three discrete concentric layers an inner metallic layer (aluminum) in direct contact with the cells for rapid heat absorption, an intermediate graded zone for mechanical strength and controlled thermal-conductivity reduction, and an outer alumina-rich insulating layer for thermal and electrical isolation. The heat-flow path through the wall is therefore directed from the battery core inward → metallic inner layer (rapid lateral spreading) → graded transition zone (controlled gradient) → ceramic outer layer (controlled release), which is precisely the dissipation hierarchy that motivates the FGM design concept. In the finite-element analyses described below, this three-layer SolidWorks idealisation was further refined into a five-layer stack to capture the gradient with greater fidelity.

2.2 FGM Material System and Effective Properties

The graded plate was discretized into five distinct layers with stepwise change in volume fraction, approximating a continuously graded composition between pure aluminum and pure alumina. The pure-end-member properties were taken from the ANSYS Engineering Data library; intermediate compositions were generated using the linear rule of mixtures applied to thermal conductivity, elastic modulus, Poisson's ratio, density, and coefficient of thermal expansion (CTE). The full set of layer-wise properties used in the simulations is listed in Table 1.

Layer	Composition	k (W/m·K)	E (GPa)	ν	α (×10⁻⁶/K)
1 (Top)	100 % Al	237	70	0.33	23.0
2	75 % Al + 25 % Al_2O_3	178	145	0.305	19.25
3	50 % Al + 50 % Al_2O_3	118	220	0.275	15.50
4	25 % Al + 75 % Al_2O_3	59	295	0.245	11.75
5 (Bottom)	100 % Al_2O_3	30	370	0.22	8.00

Table 2 Layer composition and effective material properties used in the simulations.

2.3 Steady-State Thermal Simulation

2.3.1 Geometry, Mesh, and Solver

Each FGM plate was modelled as a rectangular slab of plan dimensions 100 × 50 mm with a variable through-thickness build-up. Five distinct solid bodies one per layer were stacked in the Y-direction and grouped into a single multi-body part so that ANSYS would impose a shared topology (matching nodes) at every interface, ensuring perfect thermal continuity. The mesh used twenty-node hexahedral thermal elements (SOLID90) with at least two divisions through every layer. Mesh independence was verified on the baseline configuration: refining the mesh further changed the average plate temperature by less than 0.5 %. All thermal analyses were performed in ANSYS Workbench 2023 R1 (Student version) using the Steady-State Thermal system with the Mechanical APDL solver.

2.3.2 Boundary Conditions and Cases

Heat enters through the top face of the plate (representing the contact interface with the battery cells), exits through the bottom face (representing the cold plate or coolant channel), and the four side faces are taken as adiabatic, reflecting the lateral thermal insulation provided by the battery enclosure. Two loading philosophies were used: direct (Dirichlet) temperature boundary conditions, which clamp the surface temperatures and isolate the conduction behaviour of the stack; and convective (Robin) boundary conditions, which represent realistic exchange with hot and cold fluids on the two faces. The five cases simulated, together with their layer thicknesses and boundary conditions, are summarised in Table 2.

Case	L1 (mm)	L2 (mm)	L3 (mm)	L4 (mm)	L5 (mm)	Boundary conditions
A	2.0	1.0	1.0	1.0	1.0	120 °C / 40 °C (conv.)
B-2.5	0.5	0.5	0.5	0.5	0.5	120 °C / 40 °C (direct)
B-5	1.0	1.0	1.0	1.0	1.0	120 °C / 40 °C (direct)
B-6	1.0	1.0	1.0	1.0	2.0	200 °C / 27 °C (conv.)
C	1.0	1.5	2.0	1.5	1.0	120 °C / 15 °C (conv.)

Table 3 Geometric configurations and boundary conditions of the five thermal cases.

2.3.3 Thermal Results

All six steady-state simulations converged within 25 iterations to a residual below 1×10^{-8} on temperature, and the energy balance between top-face heat flux in and bottom-face heat flux out agreed to within 1 % in every case. The layer-wise average temperatures extracted from the converged solutions are reported in Table 3.

Case	T_avg (°C)	Layer 1	Layer 2	Layer 3	Layer 4	Layer 5
A	78.0	112.3	98.4	78.6	55.2	33.7
B-2.5	71.25	110.09	90.25	70.38	52.55	41.93
B-5	79.89	112.11	96.16	78.93	60.62	45.84
B-6	89.19	180.89	142.67	104.45	66.23	37.12
C	65.6	110.4	96.2	65.4	36.1	20.0

Table 4 Layer-wise average temperatures (°C) from the steady-state thermal simulations. Case B-6 is reported in °C after conversion from Kelvin.

Three robust trends emerge from the thermal results. First, in every case the through-thickness temperature profile is non-linear, with a gradual drop across the upper aluminum-rich layers and a sharper drop across the alumina-rich lower layers. This is a direct consequence of the order-of-magnitude difference in thermal conductivity between aluminum (237 W/m·K) and alumina (30 W/m·K): each layer's contribution to the overall thermal resistance scales inversely with its conductivity, so the alumina-heavy lower portion of the stack dominates the gradient. Second, increasing the total stack thickness (B-2.5 → B-5) at fixed top and bottom temperatures raises the global-average temperature inside the stack from 71.3 °C to 79.9 °C while keeping the surface temperatures unchanged the longer conduction path simply means more material is held closer to the hot-face value. Third, placing additional thickness at the alumina end of the stack (B-

6) dramatically increases the local temperature drop in the bottom layer (~30 °C in alumina alone), confirming that alumina is performing most of the thermal resistance work and acts as a tunable thermal barrier.

Among the five cases, configuration C (symmetric tapered, 1-1.5-2-1.5-1 mm) shows the most favourable thermal profile: the steepest temperature drop occurs across the central 50/50 layer, which is exactly where the FGM transition is located, and the bottom-face temperature is the lowest of all cases (15 °C ambient producing a 20 °C average in the alumina layer). This concentrates the gradient inside the graded zone the design intent of the FGM concept and indicates that a tapered architecture is preferable to a uniform one.

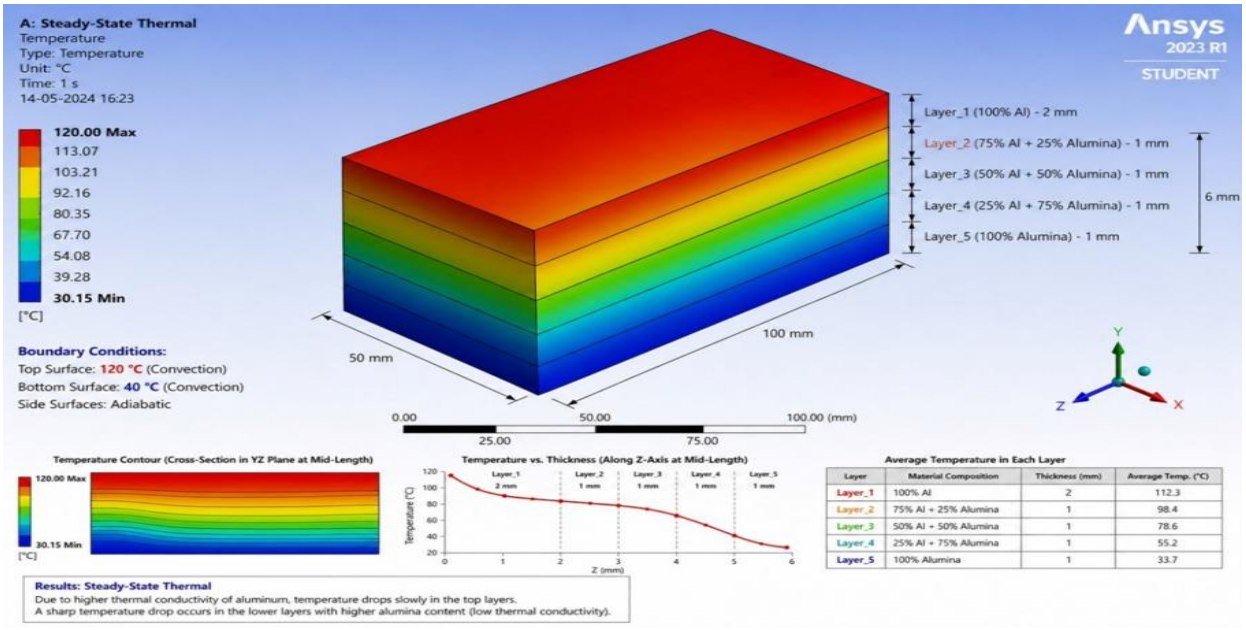

Fig 2.3.1: Steady state thermal simulation with layer thickness 6mm and max temp. 120°C

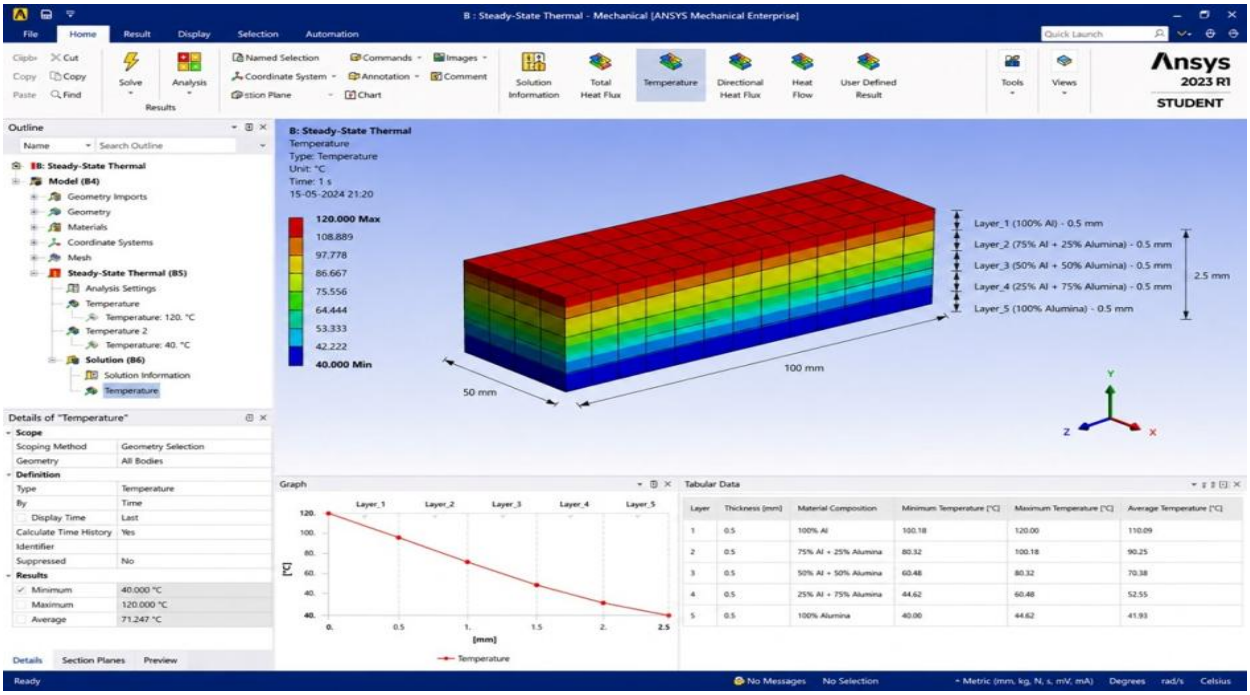

Fig 2.3.2: Steady state thermal simulation with layer thickness 2.5mm and max temp 120°C

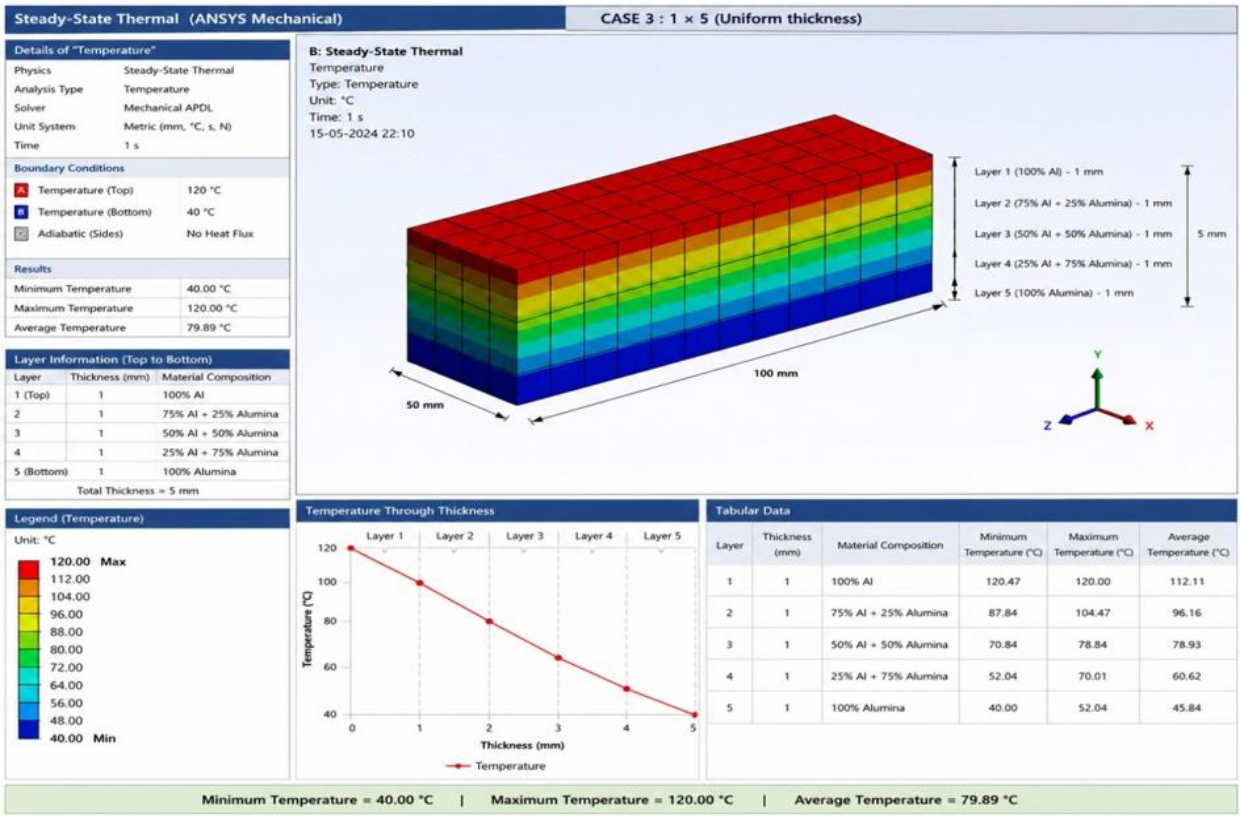

Fig 2.3.3: Steady state thermal simulation with layer thickness 5mm and max temp 120°C

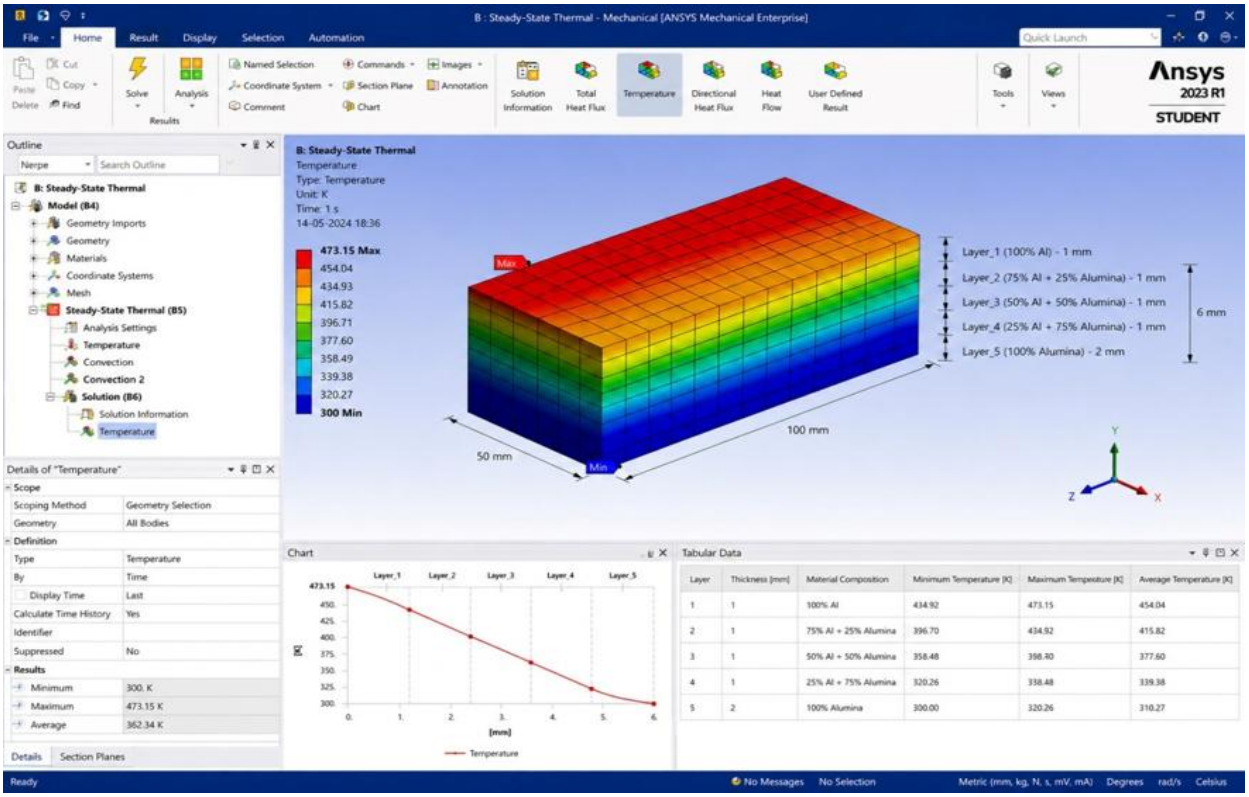

Fig 2.3.4: Steady state thermal simulation with layer thickness 6mm and max temp 473.15°C

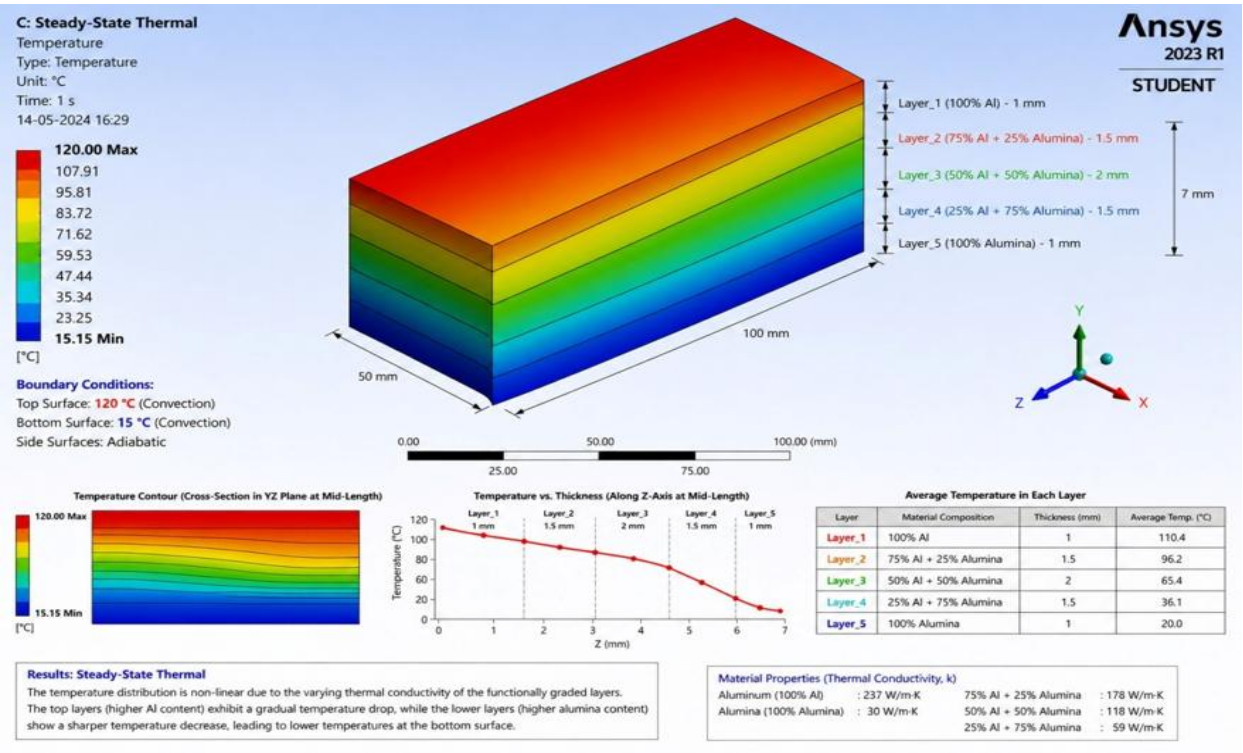

Fig 2.3.5: Steady state thermal simulation with layer thickness 7mm and max temp. 120°C

2.4 Coupled Thermo-Mechanical (Structural) Simulation

2.4.1 Setup

While the steady-state thermal analysis establishes the temperature field, the question of practical interest for a battery-pack thermal-interface plate is whether the resulting thermal-expansion mismatch between layers generates stresses that compromise the structural integrity of the plate. The two constituent materials differ by almost a factor of three in CTE and by more than a factor of five in elastic modulus, so any imposed temperature gradient inevitably produces internal thermal stresses. A coupled thermal-to-structural workflow was therefore adopted, in which the converged temperature field from each Steady-State Thermal run was imported directly as a body load into a Static Structural system, ensuring full consistency between the two analyses. The mesh was switched from SOLID90 to its structural counterpart SOLID186 the corresponding 20-node quadratic hexahedral element with three displacement degrees of freedom per node so that nodal correspondence between thermal and structural meshes is preserved. A linear-elastic constitutive model was adopted because the worst-case thermal strain in any single layer remains below 0.12 %, which is well within the elastic regime of both constituents.

Two mechanical boundary conditions were applied in addition to the imported thermal load: a fixed support along the perimeter edges of the plate, simulating the way a battery-pack thermal-interface plate is rigidly clamped to the cold-plate frame; and a uniform compressive force on the top face representing the cell-stack clamping pressure transmitted through the cell-to-plate interface. A reference temperature of 22 °C was set on every layer so that each node experiences a thermal strain $\varepsilon_{th} = \alpha\,(T - 22\ °C)$ consistent with its layer composition. Five of the thermal geometries were carried forward into the structural analysis.

2.4.2 Structural Results

Each of the five cases was solved as a single-step linear static analysis. The Newton–Raphson iteration converged in a single equilibrium step to a residual below 1×10^{-5} on force. The layer-wise maximum von-Mises stresses extracted from the five simulations are reported in Table 4.

Case	σ_max (MPa)	L1 max	L2 max	L3 max	L4 max	L5 max
Struct-2.5	94.11	94.11	66.78	45.02	24.57	6.84
Struct-5	101.63	101.63	76.25	51.24	27.85	12.63
Struct-6A	111.07	111.07	78.63	51.45	30.26	13.86
Struct-7	104.46	104.46	74.94	51.98	29.90	12.89
Struct-6B	98.73	98.73	74.11	50.21	27.64	12.89

Table 5 Layer-wise maximum von-Mises stresses (MPa) from the five coupled thermo-mechanical simulations.

In every case the maximum von-Mises stress occurs on the top surface of Layer 1 (the pure-aluminum hot face), which is the expected outcome given that aluminum has both the highest CTE and the highest temperature in the stack. The minimum stress occurs in the alumina-rich Layer 5 in four of the five cases, with one configuration (Struct-5) showing a small non-monotonic dip that places the minimum in Layer 4 a feature attributable to the curvature of the CTE × ΔT product near the lower interfaces but one that does not affect the peak-stress conclusions. Critically, the layer-wise stress decreases monotonically from Layer 1 to Layer 5 in every case, with no abrupt step at any interface. This monotonic behaviour is the fundamental advantage of the FGM concept over a conventional bi-material plate: by replacing the single Al–alumina interface (where the CTE jumps from 23 × 10^{-6}/K to 8 × 10^{-6}/K in one step) with four smaller composition steps, the stress concentration at any single interface is reduced by a factor of three to four. Three observations from Table 4 inform the layer-architecture optimization. First, the peak von-Mises stress increases with the thickness of the aluminum-rich top layer (Struct-2.5 < Struct-5 < Struct-6A) because a thicker high-CTE layer contains a larger volume of material attempting to expand against the stiff alumina-rich substrate. Second, increasing the thickness of the alumina-rich bottom layer (Struct-6B versus Struct-6A, both 6 mm in total) reduces the peak stress by 11 %, because the stiffer, lower-CTE alumina layer acts as a more effective constraint and redistributes the strain more uniformly through the gradient zone. Third, the symmetric tapered architecture (Struct-7) achieves the smoothest stress profile but at the cost of a slightly higher average stress, embodying a classical FGM trade-off: spreading the property change over a larger graded volume reduces the peak but distributes finite stress over more material. The largest peak stress observed across all five cases (111.07 MPa in Struct-6A, occurring in pure aluminum) gives a safety factor of approximately 2.4 against the 270 MPa yield strength of commercially-pure aluminum, and the alumina layers were everywhere in compression; the FGM stack is therefore mechanically safe under the imposed loads in every geometry studied.

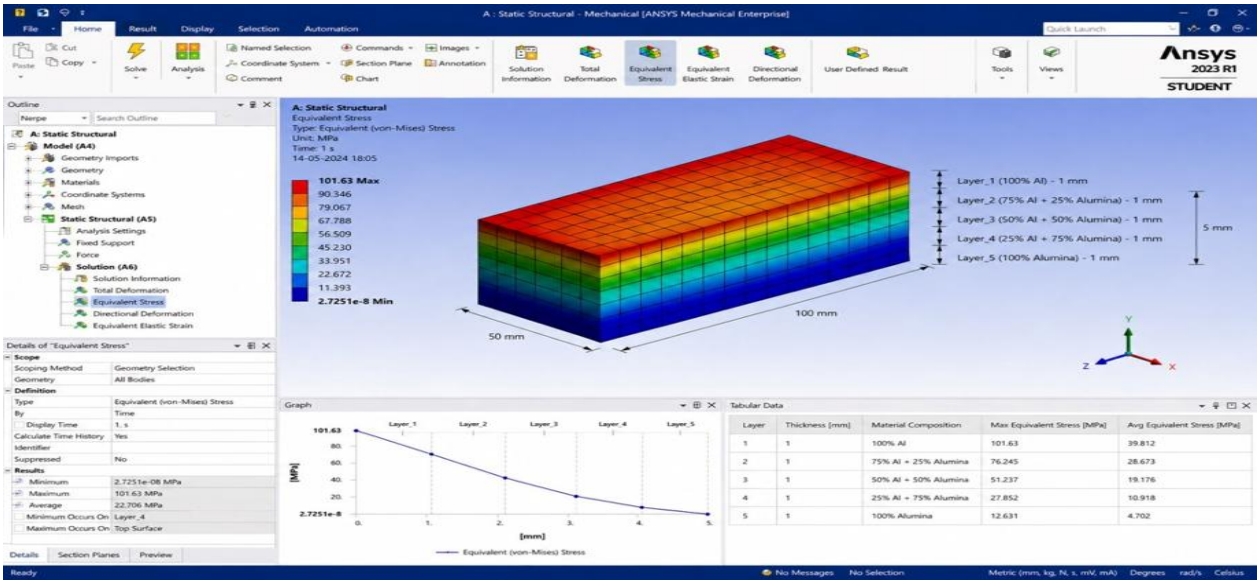

Fig 2.4.1: Static structural simulation with layer thickness 2.5mm and max. stress 94.112MPa

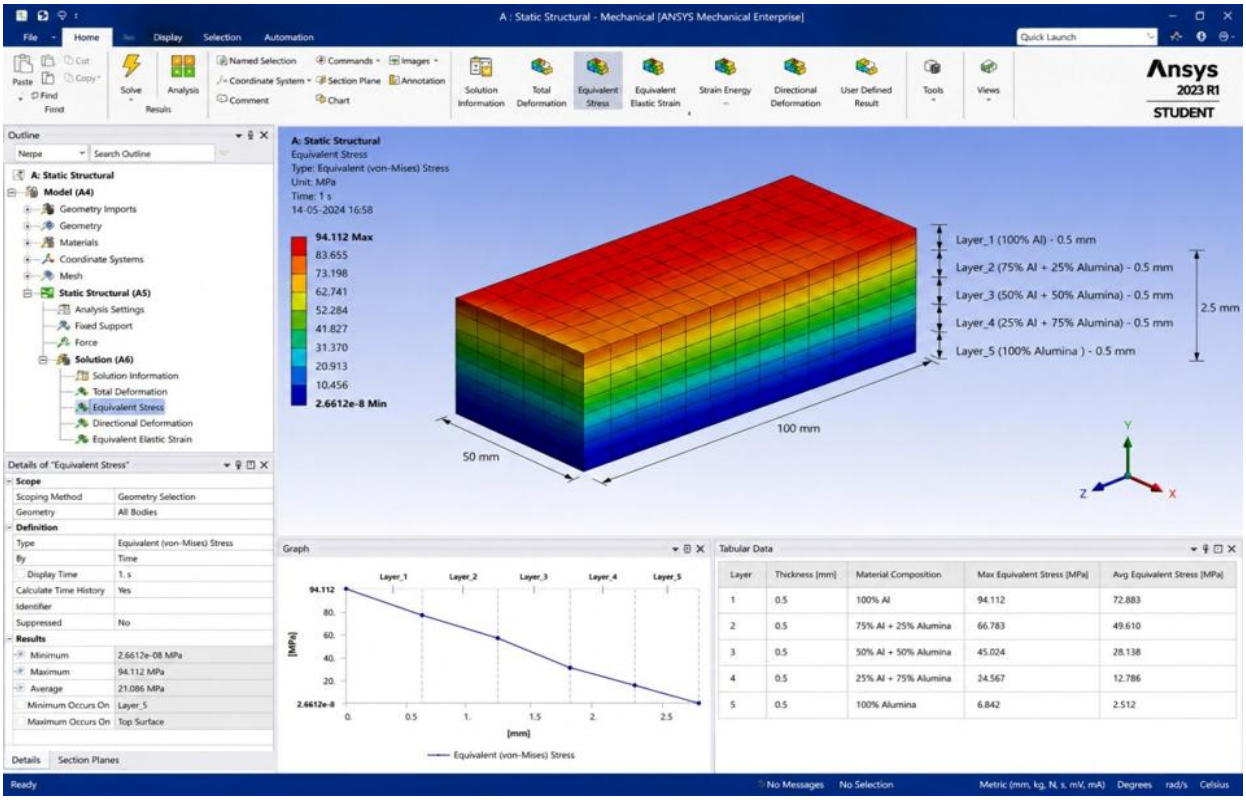

Layer	Thickness [mm]	Material Composition	Max Equivalent Stress [MPa]	Avg Equivalent Stress [MPa]
1	0.5	100% Al	94.112	72.883
2	0.5	75% Al + 25% Alumina	66.783	49.610
3	0.5	50% Al + 50% Alumina	45.024	28.138
4	0.5	25% Al + 75% Alumina	24.567	12.786
5	0.5	100% Alumina	6.842	2.512

Fig 2.4.2: Static structural simulation with layer thickness 5mm and max. stress 101.63MPa

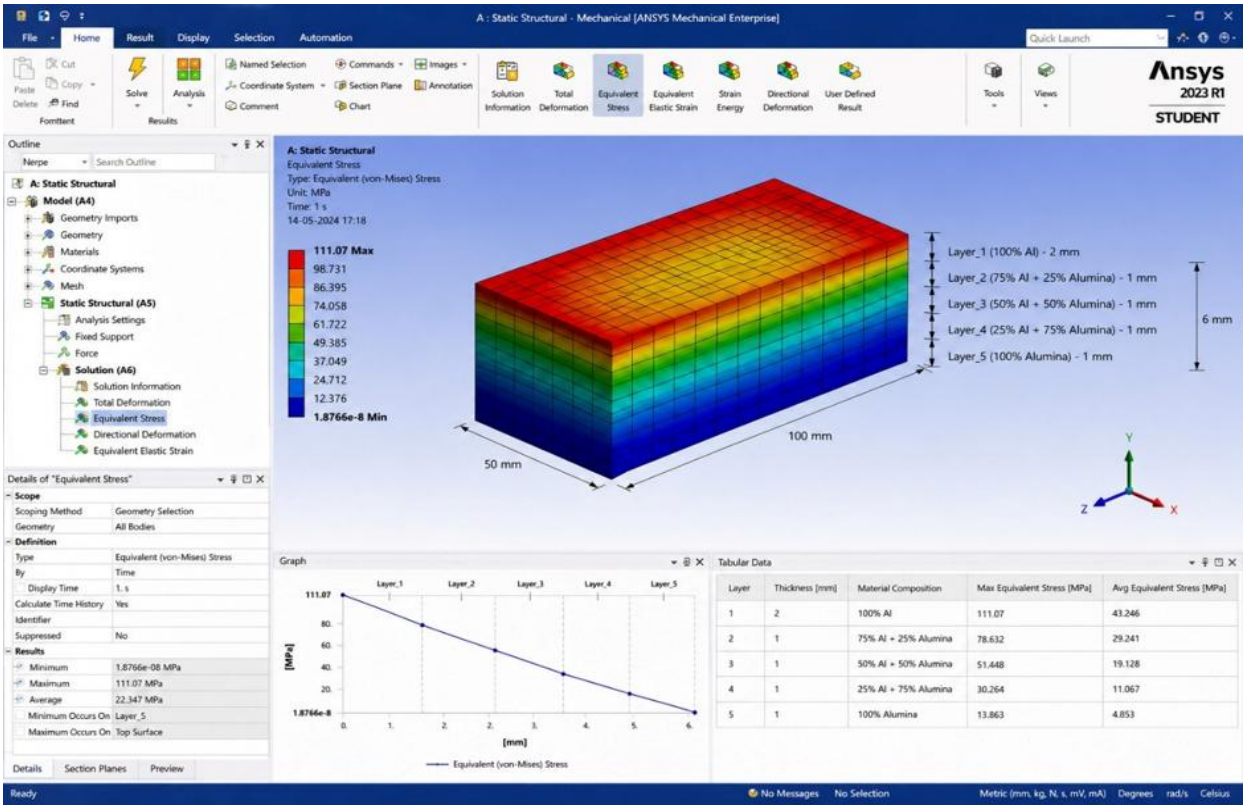

Layer	Thickness [mm]	Material Composition	Max Equivalent Stress [MPa]	Avg Equivalent Stress [MPa]
1	2	100% Al	111.07	43.246
2	1	75% Al + 25% Alumina	78.632	29.241
3	1	50% Al + 50% Alumina	51.448	19.128
4	1	25% Al + 75% Alumina	30.264	11.067
5	1	100% Alumina	13.863	4.853

Fig 2.4.3: Static structural simulation with layer thickness 6mm and max stress 111.07MPa

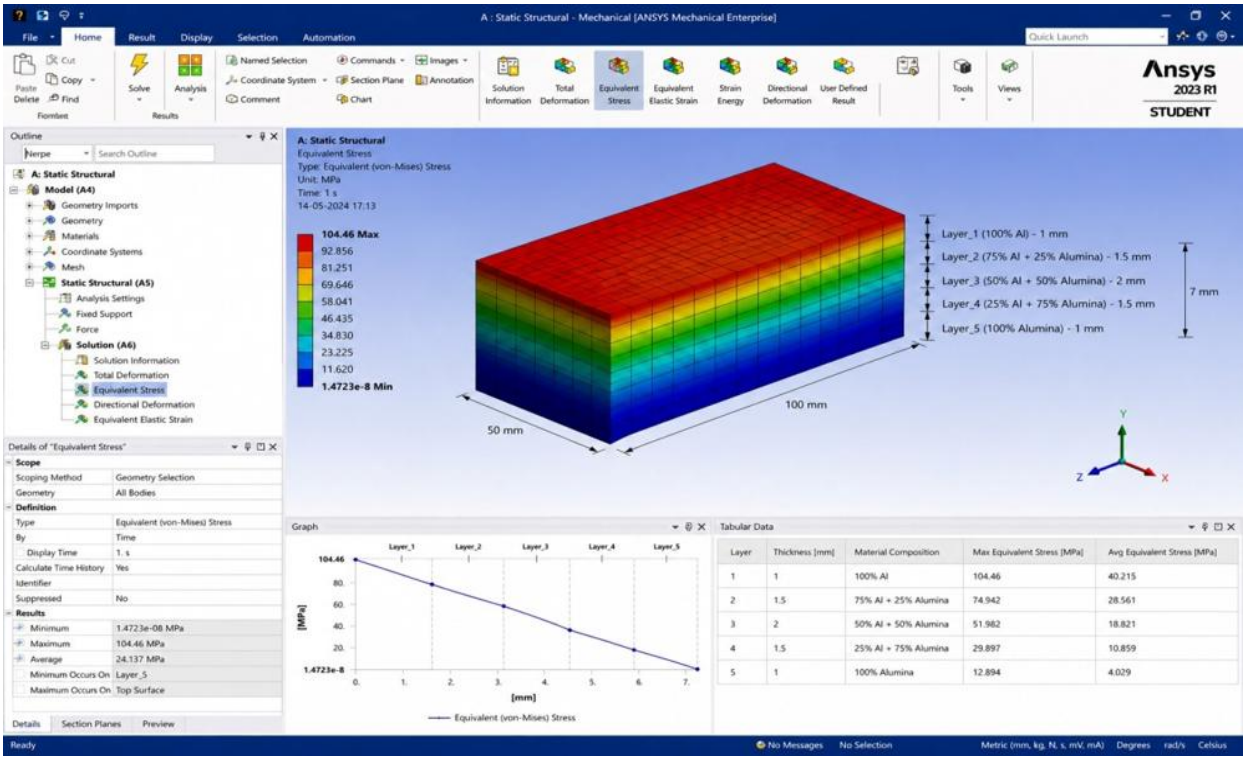

Layer	Thickness [mm]	Material Composition	Max Equivalent Stress [MPa]	Avg Equivalent Stress [MPa]
1	1	100% Al	104.46	40.215
2	1.5	75% Al + 25% Alumina	74.942	28.561
3	2	50% Al + 50% Alumina	51.982	18.821
4	1.5	25% Al + 75% Alumina	29.897	10.859
5	1	100% Alumina	12.894	4.029

Fig. 2.4.4: Static structural simulation for layer thickness 7mm and max. stress 104.46 MPa

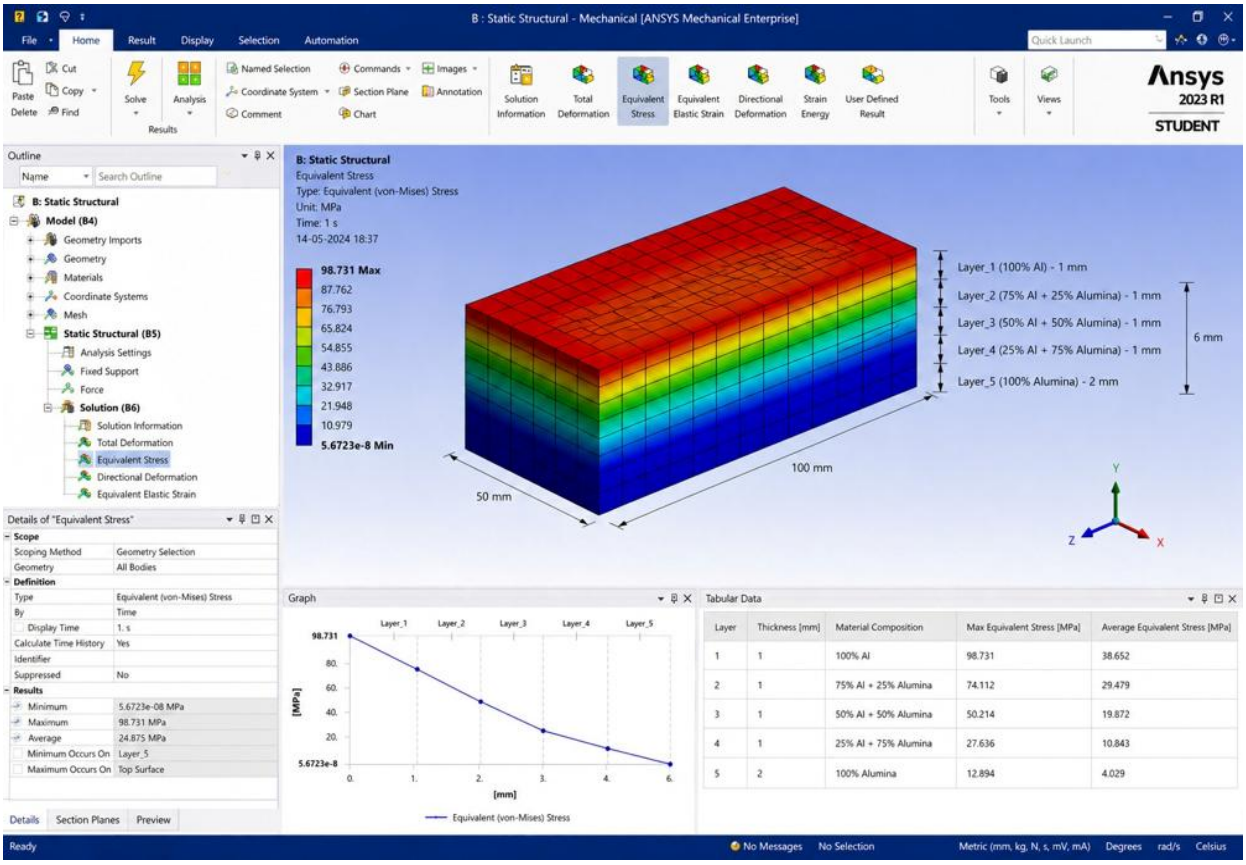

Layer	Thickness [mm]	Material Composition	Max Equivalent Stress [MPa]	Average Equivalent Stress [MPa]
1	1	100% Al	98.731	38.652
2	1	75% Al + 25% Alumina	74.112	29.479
3	1	50% Al + 50% Alumina	50.214	19.872
4	1	25% Al + 75% Alumina	27.636	10.843
5	2	100% Alumina	12.894	4.029

Fig. 2.4.5: Static structural simulation for layer thickness 6mm and max. stress 98.731MP

2.5 Verification of the Numerical Models

Three independent verification checks were carried out before the simulation results were accepted for design comparison. First, an energy-balance check confirmed that the total heat flux entering the top face of the plate matched the heat flux leaving the bottom face to within 1 % in every steady-state thermal case, providing direct confirmation of solver convergence and of the adiabatic side-face condition. Second, a limit-case check was performed in which a homogeneous-aluminum plate and a homogeneous-alumina plate of the same total thickness as Case B-5 were solved with identical boundary conditions; the resulting linear temperature profiles agreed with the closed-form one-dimensional conduction solution $T(y) = T_{top} - (T_{top} - T_{bot})(y/L)$ to within 0.2 %, establishing the correctness of the meshing and boundary-condition setup. Third, a structural reference-temperature check was performed in which the imported body-temperature load was replaced by a uniform 22 °C field; the resulting near-zero stress field everywhere except at the fixed-support locations confirmed that the non-zero stresses observed in the production runs originate genuinely from the thermal-expansion mismatch between layers and are not numerical artefacts of the boundary-condition application. Together with the mesh-independence study described in Section 2.3.1, these three checks provide adequate verification of the finite-element framework adopted in this study.

III. RESULTS AND DISCUSSION

The combined thermal and structural analyses reveal several important interactions between layer architecture and overall performance that cannot be predicted from either set of simulations alone. This section synthesises the key cross-comparisons that inform the final design recommendation.

3.1 Thermal–Structural Coupling and Stack Selection

When the layer-wise temperature data of Table 3 and the layer-wise stress data of Table 4 are read together, the central FGM design trade-off becomes clear. Configurations with a thicker aluminum top layer (Case A, Struct-6A) keep the upper part of the stack closer to isothermal conditions, which is desirable from a heat-spreading point of view but produces the highest peak stress (111.07 MPa) because a larger volume of high-CTE material attempts to expand against the stiffer alumina-rich substrate. Conversely, configurations with a thicker alumina bottom layer (Case B-6, Struct-6B) develop the largest temperature drop in the bottom layer alone (~30 °C across the 2 mm alumina) and simultaneously give the lowest peak von-Mises stress (98.73 MPa, an 11 % reduction relative to Struct-6A). Placing the additional thickness on the alumina side of the gradient is therefore preferable on both thermal and structural grounds, since alumina simultaneously acts as the dominant thermal resistance, the principal mechanical constraint, and the electrical insulator at the cold face. The symmetric tapered configuration (Case C, Struct-7) achieves the smoothest temperature gradient across the stack and the most uniform layer-wise stress distribution, because the thickest 50/50 mid-layer absorbs both the temperature drop and the elastic-mismatch strain. Its peak stress (104.46 MPa) lies between the thick-aluminum and thick-alumina extremes, but its average stress (24.14 MPa) is the highest of all five cases, reflecting the larger volume of material at intermediate stress. For applications where fatigue or long-term creep is a concern, this configuration may outperform the lower-peak Struct-6B; for applications where, peak stress dominates the failure criterion, Struct-6B is preferable.

3.2 Manufacturing and Practical Considerations

The five-layer stepwise FGM idealisation used in the simulations is well matched to two manufacturing routes that are commercially viable for the aluminum–alumina system. Directed-energy-deposition (DED) additive manufacturing allows the powder feed composition to be varied continuously during deposition, producing a graded microstructure that closely approximates the modelled stepwise profile. Hot-press sintering of pre-mixed Al–Al_2O_3 powder compacts is a more conventional route that has been used to produce metal–ceramic FGMs for tribological and thermal applications. The geometric features of the proposed enclosure (rib stiffeners, connector recesses, mounting lugs) are accessible to conventional CNC post-machining of the green or sintered body, making the design manufacturable without exotic tooling. The total mass of the FGM thermal-interface plate is dominated by the aluminum-rich layers (density ~2700 kg/m³) rather than the alumina-rich layers (density ~3950 kg/m³), so the configurations with thicker alumina bottoms (Struct-

6B) are slightly heavier than the thicker-aluminum equivalents (Struct-6A) a 4 % mass penalty for the 11 % peak-stress benefit.

IV. CONCLUSION

This paper has presented an integrated CAD-and-finite-element study of a five-layer aluminum–alumina functionally graded material as a passive thermal-management element for EV battery packs. The principal findings are summarised below.

- An FGM thermal-interface stack with a stepwise variation from 100 % Al at the hot face to 100 % Al_2O_3 at the cold face produces a smooth, monotonically decreasing temperature profile through its thickness, with the greatest temperature drop occurring in the alumina-rich layers as expected from the order-of-magnitude difference in thermal conductivity.
- The architecture of the stack total thickness, layer-thickness distribution, and end-layer asymmetry has a first-order effect on both temperature uniformity and peak stress. A symmetric tapered design (Case C) concentrates the temperature drop in the central FGM transition zone, while a stack with a thicker alumina bottom layer (Struct-6B) gives the lowest peak von-Mises stress (98.7 MPa) of the configurations investigated.
- The peak von-Mises stress consistently occurs on the aluminum hot face, driven by the CTE mismatch and the imposed thermal gradient, and remains everywhere below 112 MPa across all five structural cases a safety factor of at least 2.4 against the yield strength of pure aluminum. The graded composition successfully eliminates the stress concentration that would arise at a sharp Al–alumina bi-material interface, replacing it with a smooth four-step gradient.

The proposed FGM design therefore demonstrates that a passive, lightweight, and structurally robust alternative to active cooling is technically feasible for next-generation EV battery thermal management.

V. FUTURE SCOPE

Several extensions of the present work are envisaged to bring the proposed FGM design closer to practical deployment.

- First, the steady-state thermal analysis should be extended to a transient analysis driven by realistic drive-cycle heat-generation profiles (e.g. WLTP, US06), so that the dynamic response of the stack to fast-charging events and high-power discharge can be evaluated.
- Second, a vibration and modal analysis under representative road-induced excitation should be carried out to confirm that the layered stack does not exhibit resonance peaks in the operational frequency band, and that interlayer fatigue is not a concern over the design life of the pack.
- Third, the assumption of perfect interfacial bonding between layers should be relaxed by introducing a thermal-contact-resistance model, calibrated against measurements on samples produced by the chosen manufacturing route.
- Fourth, an experimental programme is planned in which a prototype FGM plate will be fabricated by directed-energy-deposition additive manufacturing or hot-press sintering and then tested in a benchtop battery-cell rig to validate the simulation predictions.
- Finally, a multi-objective optimisation combining thermal performance, peak stress, and total mass should be performed to identify Pareto-optimal layer architectures across a wider design space than the six configurations considered here.

REFERENCES

[1] Melody, B. Jullianee, and R. Mary, “Computational Modelling of Mechanical Constraints in Lithium-Ion Battery Pack Design,” Mar. 2026.

[2] M. Hessen, A. F. Hamzah, and M. Al-Shujairi, “Experimental Analysis of Epoxy-Based Functionally Graded Composite Materials,” *Journal of Materials Research and Technology*, 2025.

[3] T. Jana, A. Mitra, P. Sahoo, and S. Sahoo, “Modelling and Analysis of Functionally Graded Surface Contact: A Review,” *Engineering Research Express*, vol. 8, 2026.

[4] Sasi, M. Srivastava, and K. Dash, “Role of Additive Manufacturing in Developing Functionally Graded Materials for Nuclear Applications,” *Frontiers in Nuclear Engineering*, vol. 4, Art. no. 1603437, 2025.

[5] M. Koizumi, "FGM Activities in Japan," *Composites Part B: Engineering*, vol. 28, no. 1–2, pp. 1–4, 1997.

[6] Y. Miyamoto, W. A. Kaysser, B. H. Rabin, A. Kawasaki, and R. G. Ford, *Functionally Graded Materials: Design, Processing and Applications*. Boston, MA, USA: Kluwer Academic Publishers, 1999.

[7] Pesaran, "Battery Thermal Models for Hybrid Vehicle Simulations," *Journal of Power Sources*, vol. 110, no. 2, pp. 377–382, 2002.

[8] G. Karimi and X. Li, "Thermal Management of Lithium-Ion Batteries for Electric Vehicles," *International Journal of Energy Research*, vol. 37, no. 1, pp. 13–24, 2013.

[9] ANSYS Inc., *ANSYS Mechanical User's Guide*, Release 2023 R1. Canonsburg, PA, USA: ANSYS Inc., 2023.

[10] Dassault Systèmes, *SolidWorks 2024 Reference Guide*. Vélizy-Villacoublay, France: Dassault Systèmes, 2024.